Engineering Fracture Mechanics 236 (2020) 107214

Contents lists available at ScienceDirect

Engineering Fracture Mechanics

journal homepage: www.elsevier.com/locate/engfracmech

# A new fatigue reliability analysis method for steel bridges based on peridynamic theory

Yingkai Liu[a], Lu Deng[a,*], Wenjie Zhong[a], Jun Xu[a], Wen Xiong[b]

[a] Department of Civil Engineering, Hunan University, China
[b] School of Transportation, Southeast University, China

ARTICLE INFO

*Keywords:*
Peridynamics
Steel bridge
Fatigue crack
Reliability
Biaxial loading

ABSTRACT

A fatigue reliability model based on the peridynamic (PD) theory was proposed to analyze the fatigue performance of steel bridges in this study. Different from previous methods based on classical continuum mechanics, the PD model does not require additional criteria to guide the growth of crack or damage. In particular, the influence of fatigue threshold value was considered in a systematic formula, and the response surface method was utilized to analyze fatigue failure probability. The proposed model was applied to complex fatigue phenomena such as spontaneous crack nucleation, crack branching, and fatigue failure under biaxial cyclic loadings where fatigue crack paths interact in complicated ways. The fatigue crack growth pattern, fatigue life, and fatigue reliability of specimens considering the biaxial or uniaxial fatigue loadings were analyzed. The accuracy of the fatigue model was verified through a series of comparisons with the experimental, analytical, and FEM results. The effectiveness of the proposed method was also demonstrated in the application to the fatigue reliability analysis of the Ting Kau Bridge.

## 1. Introduction

With the widespread applications of steel bridges, the assessment of their residual fatigue lives has become an important issue [1–3]. To obtain an accurate prediction of the residual fatigue life of steel bridges, various factors, e.g., vehicle overload, increasing traffic volume and structural components with unknown fatigue property, need to be considered, which is essential for conducting structural replacements [4–5]. One important issue in steel bridges is the crack development. Recently, a number of bridge accidents occurred in different countries indicate that the cracks appearing at welded details can significantly reduce the fatigue life of steel bridges [6–8]. The cracks are random in nature and thus pose a difficulty in the fatigue life prediction.

To date, plenty of researches on the fatigue life evaluation of reinforced concrete and steel bridges have been carried out [9–17]. For example, Bolzon and Corigliano [15] proposed a general mixed finite element method (FEM) to model the nucleation and spread of discrete cracks. Stazi et al. [16] used enriched quadratic interpolations in their FEM formulation to resolve the singular stress field at crack tips, which is able to treat linear elastic fracture mechanics problems without significant mesh refinement. However, there remain some defects in these approaches. As pointed out by Shen et al. [17], discontinuous stress and strain formed at crack tips should be dealt with by special singularity processing in FEM. Conventionally, external crack propagation criteria were introduced to regulate the crack, but they may fail when dealing with complex crack paths. Recently, a cohesive zone model [18] was proposed for the purpose of improving the conventional FEM, but it still requires a prior knowledge of the crack propagation path. Therefore, it is acknowledged that the current FEM practice of fatigue life prediction of steel bridges suffers from discontinuous stress and strain

* Corresponding author.
*E-mail address:* denglu@hnu.edu.cn (L. Deng).

https://doi.org/10.1016/j.engfracmech.2020.107214
Received 25 February 2020; Received in revised form 14 June 2020; Accepted 15 July 2020
Available online 20 July 2020
0013-7944/ 

fields which require special treatment of singularities and therefore cannot fully incorporate crack initiation and propagation. Besides, fatigue failure is a dynamic process, meaning that remeshing is required in the simulation which makes the issue more difficult.

In order to overcome the shortcomings of traditional FEM, Silling [19] develop the PD theory which does not assume spatial differentiability of displacement field and permits discontinuities to arise as part of solution. PD has been utilized successfully for progressive cracking and failure prediction in various situations, e.g., impact issue [20], composite damage [21], metal corrosion [22].The PD theory was first applied to the fatigue life evaluation by Silling and Askari [23]. Their model is capable of simulating the three phases of fatigue failure, i.e., crack nucleation, fatigue growth and failure in a quasi-static crack growth sample. Silling and Askari [23] also modeled the nucleation of a fatigue crack at a stress concentration and its growth along a curved trajectory in three dimensions under quasi-static condition by using the dynamic relaxation method. They indicated that the PD theory is advantageous in simulating spontaneous formation, interaction and growth of discontinuities in a consistent framework, and thus provides a way to treat the fatigue crack nucleation and growth as part of a consistent mathematical description of the boundary value problem while no additional criteria for crack growth process is needed. Oterkus et al. [24] developed a methodology to predict the fatigue failure of materials, in which a PD parameter related to the crack growth, i.e., the critical bond stretch, is assumed to degrade exponentially with the cyclic load progress. Jung and Seok [25] extended the PD fatigue model to a mixed-mode case, and the proposed model was verified by experimental results to be able to predict the fatigue life of specimens under various load conditions with high accuracy.

In the present work, a new reliability method based on PD theory for predicting the fatigue crack behavior of steel bridges under quasi-static condition is proposed. The new method incorporates the material failure intrinsically and can therefore avoid the need for external crack growth criteria and post-processing. Moreover, a response surface method is utilized in the fatigue calculation of steel bridges under vehicle loading to evaluate the inherent uncertainties in fatigue problems, as introduced in Section 2.3. The accuracy of the proposed method is verified via comparing the simulation results with both the experimental and analytical results. In a case study, the new method is applied to an actual steel bridge, in which a structural health evaluation system is established to evaluate the fatigue failure probability of the thin-walled members and the fatigue performance of the bridge under actual vehicle loadings.

## 2. Peridynamic theory for fatigue failure

### 2.1. Brief review of two-dimensional (2D) bond-based PD model

The PD theory can be considered as an extension of molecular dynamics in continuum dynamics, which makes the property of a continuum effectively treated from the perspective of submicroscopic. As schematically depicted in Fig. 1, in PD theory, a material domain is discretized into a finite number of particles, which interact with each other by means of internal forces. The mass of individual particles is calculated based on the equal share of mass between neighboring particles and their locations are determined by integrating the equations of motion. The internal forces between particles are calculated by the empirical interaction function. Particles move in accordance with Newton's second law and take the form as

$$\rho\ddot{\mathbf{u}}(\mathbf{x},t)=\int_{\mathbf{H}}f(\mathbf{u}(\mathbf{x},t)-\mathbf{u}(\mathbf{x}',t),\mathbf{x}-\mathbf{x}')dV_{\mathbf{x}'}+\mathbf{b}(\mathbf{x},t)\tag{1}$$

where ρ is the spatially dependent density; **u** is the displacement vector; *f* is the pairwise force function of the PD bond that connects particles **x** and **x′**; **b**(**x**,*t*) is the body force; The integral range **H** represents the compact supported region of the pairwise force function around particle **x** (see Fig. 1), and is called the "horizon region" or simply named as "horizon". This horizon domain is a spherical neighborhood of the central particle **x**, but excluding **x**, with its mathematical expression given as

$$\mathbf{H}=\{\mathbf{x}'\in R|0<|\mathbf{x}-\mathbf{x}'|\le\delta\}\tag{2}$$

In the case of a micro-elastic material, the pairwise force function between particles **x** and **x′** is defined as

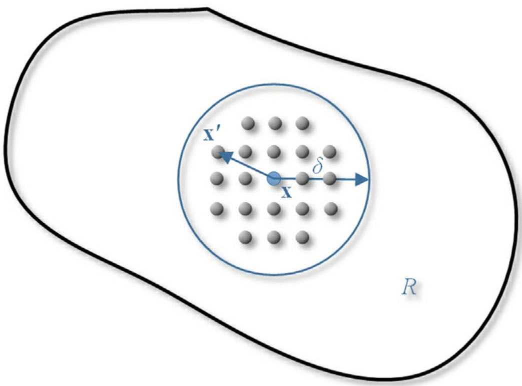


**Fig. 1.** Pairwise interaction of a material particle **x** with its neighboring particle **x′**.

$$f(\boldsymbol{\eta},\boldsymbol{\xi})=\begin{cases}\frac{\boldsymbol{\eta}+\boldsymbol{\xi}}{|\boldsymbol{\eta}+\boldsymbol{\xi}|}c(\xi)s & \xi\le\delta\\ 0 & \xi>\delta\end{cases} \tag{3}$$

where $\boldsymbol{\eta}(=\mathbf{u}'\text{-}\mathbf{u})$ and $\boldsymbol{\xi}(=\mathbf{x}'\text{-}\mathbf{x})$ represent the relative position in the configuration and the relative displacement between $\mathbf{x}$ and $\mathbf{x}'$, respectively. Note that the direction of $f$ is parallel to the relative position vector at the deformed state ($\boldsymbol{\eta}+\boldsymbol{\xi}$). The micromodulus function $c(\xi)$ is determined by equating the PD internal energy of a body with the strain energy density derived from the classical elasticity theory under the same deformation. There are two types of micromodulus function $c(\xi)$ in 1D plane-stress condition, i.e., the constant one and the conical one [26]. The same procedure has also been employed to calculate $c(\xi)$ in 2D condition [27]. The following equations, both of which are obtained under plane-stress conditions, are for the conical micromodulus function and constant micromudulus function in 2D, respectively.

$$c(\xi)=c_1\left(1-\frac{\xi}{\eta}\right)=\frac{24E}{\pi\delta^3(1-\nu)}\left(1-\frac{\xi}{\eta}\right) \tag{4}$$

$$c(\xi)=c_0=\frac{6E}{\pi\delta^3(1-\nu)} \tag{5}$$

where $E$ is Young's modulus and $\nu$ is Poisson's ratio. Note that $\xi=||\boldsymbol{\xi}||$, $\eta=||\boldsymbol{\eta}||$, and $s$ in Eq. (3) is the bond's relative stretch which is defined in terms of relative position $\boldsymbol{\xi}$ and relative displacement $\boldsymbol{\eta}$ as

$$s=\frac{|\boldsymbol{\xi}+\boldsymbol{\eta}|-|\boldsymbol{\xi}|}{|\boldsymbol{\xi}|} \tag{6}$$

When the relative elongation of a bond exceeds a critical value $s_0$, breakage occurs between a pair of particles and as a consequence, the two particles will no longer interact and cause material damage. The internal force on this bond is simply replaced by zero.

$$f(\boldsymbol{\eta}+\boldsymbol{\xi})=\begin{cases}f(\boldsymbol{\eta},\boldsymbol{\xi}) & s\le s_0\\ 0 & s>s_0\end{cases} \tag{7}$$

The critical relative elongation $s_0$ is computed based on the fracture energy of material. In 2D, the fracture energy $G_0$ is defined as the energy per unit fracture length for completely separating a body in two halves. Equating $G_0$ with the fracture energy derived from the PD theory, we have

$$G_0=2\int_0^{\delta}\int_z^{\delta}\int_0^{\cos^{-1}\left(\frac{z}{\xi}\right)}\left[\frac{c(\xi)c_0^2\xi}{2}\right]\xi d\theta d\xi dz \tag{8}$$

Substituting the micromodulus function derived from Eqs. (4) and (5) into Eq. (8), $s_0$ is obtained as:

$$s_0=\sqrt{\frac{5\pi G_0}{9E\delta}} \tag{9}$$

for the conical micromodulus function and

$$s_0=\sqrt{\frac{4\pi G_0}{9E\delta}} \tag{10}$$

for the constant micromodulus function.

### 2.2. PD fatigue model

For elastic-brittle materials, the PD constitutive equation of motion, as shown in Eq. (1), can be rewritten as

$$f(\boldsymbol{\eta},\boldsymbol{\xi},\varphi,t)=\begin{cases}f(\boldsymbol{\eta},\boldsymbol{\xi},\varphi,t) & \text{if}\ \ s(\boldsymbol{\xi},t')\le s_0\ \ \text{and}\ \ \varphi>0\ \ \text{for}\ \ 0\le t'\le t\\ 0 & \text{otherwise}\end{cases} \tag{11}$$

where $\varphi$ is adopted to represent the remaining fatigue life of a given bond. $\varphi$ is set to 1 when the bond is intact, and will decrease monotonically to 0 with the increase of cycling numbers $N$. Fatigue fracture will happen when the bond has no remaining fatigue life, $\varphi(N)=0$.

Comparing with Paris law, the relationship between fatigue life decay rate and strain amplitude can be expressed in Eq. (12).

$$\begin{cases}\frac{d\varphi}{dN}(N)=-\gamma(\varepsilon)\varepsilon^{m_1}=-(n\varepsilon+c)\varepsilon^{m_1}\\ \qquad\qquad \varphi(0)=1\end{cases} \tag{12}$$

Here, $\varepsilon=|s^+\text{-}s^-|$ is the current cyclic bond strain, $\gamma(\varepsilon)$ is a positive parameter determined by the bond strain $\varepsilon$, while $m_1$ is a positive constant exponent. Note that the effect of mean stress/strain effect was not obvious in simple fatigue example, while the mean probability density function model was very difficult to be obtained in a complex engineering problem. Therefore, only the amplitude

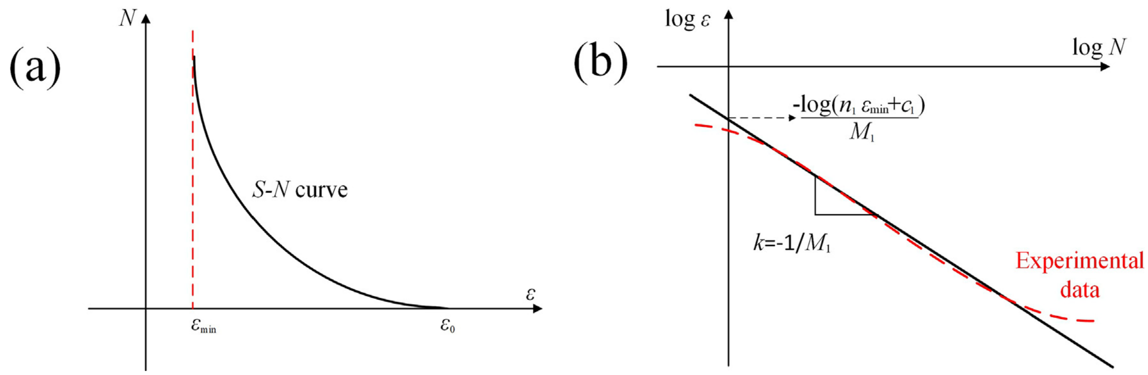


**Fig. 2.** Loading cycles $N$ as a function of bond strain $\varepsilon$.

effect is considered and the effect of mean stress/strain is ignored. The bond break immediately when the fatigue life $\varphi$ is less than or equal to 0, and the broken bond will no longer interact with others. Note that the cycle number $N$ is recommended to be treated as a real number instead of an integer [23].

In the fatigue crack nucleation phase, $\gamma(\varepsilon)$ and $m_1$can be assumed as

$$\gamma_1(\varepsilon) = n_1\varepsilon + c_1,\ m_1 = M_1 - 1 \tag{13}$$

where $n_1$, $c_1$ and $M_1$ are positive constants independent of nodes position and cyclic number, and are determined by the real material properties from experiments. In order to compute the critical cycle number $N_1$ exceeding which the bond will break, Eq. (12) is integrated over $N$.

$$(n_1\varepsilon_1 + c_1)\varepsilon_1^{M_1-1}\cdot N_1 = 1 \tag{14}$$

In Eq. (14), the bond strain $\varepsilon_1$ is assumed independent of $N$. Two key values, i.e., $\varepsilon_0$ and $\varepsilon_{\min}$, found in the $S$-$N$ curve as plotted in Fig. 2 (a) denote the critical bond stain and the threshold bond strain respectively. In log–log as shown in Fig. 2(b), the slope $k = -1/M_1$. When the bond strain $\varepsilon_1$ is set as $\varepsilon_0$ and $\varepsilon_{\min}$, Eq. (14) can be rewritten as

$$\begin{cases} (n_1\varepsilon_0 + c_1)\varepsilon_0^{M_1-1} = 1, & \varepsilon = \varepsilon_0 \\ (n_1\varepsilon_{\min} + c_1)\varepsilon_{\min}^{M_1-1} = 0, & \varepsilon = \varepsilon_{\min} \\ M_1 = -\frac{1}{k} & \end{cases} \tag{15}$$

from which $n_1$ and $c_1$ can be obtained.

$$\begin{cases} n_1 = \frac{\varepsilon_0^{1/k+1}}{\varepsilon_0 - \varepsilon_{\min}} \\ c_1 = -\frac{\varepsilon_0^{1/k+1}}{\varepsilon_0 - \varepsilon_{\min}}\cdot\varepsilon_{\min} \end{cases} \tag{16}$$

For some materials, no fatigue damage will occur when the fatigue strain is less than a certain threshold ($\varepsilon_{\min}$ in $S$-$N$ curve). However, in some cases, any minor strain should not be ignored in fatigue accumulation, which means that the threshold value $\varepsilon_{\min} = 0$ and Eq. (14) can be rewritten as

$$\begin{cases} n_1 = \varepsilon_0^{1/k} \\ c_1 = 0 \end{cases} \tag{17}$$

A special case of Eq. (14) can be obtained when substituting $n_1$ and $c_1$back into Eq. (14), which is the same as the critical fatigue life equation given in [23] and [28]. Although Silling and Askari [23] also considered the influence of threshold value $\varepsilon_{\min}$, but the threshold value is not directly reflected in the systematic formula. We explain the derivation process here in detail, and give a general solution of PD fatigue model.

When the fatigue cycle number $N > N_1 = 1/(n_1\varepsilon_1 + c_1)\varepsilon_{m1}$, the crack nucleates. During the nucleation phase, when at least one bond breaks, quasi-static analysis should be performed immediately and a new stress field is calculated in the same cycle. If non-fatigue fracture occurs, the quasi-static calculation should be repeated in the cycle until the non-fatigue fracture no longer occur. Then the next fatigue cycle is started, and it is ended with occurrence of a new fatigue fracture on the bond with strain $\varepsilon \geq \varepsilon_1$. The quasi-static analysis method is again utilized to calculate the stress field in the new cycle. The stress relaxation method [29] is used here for the quasi-static analysis.

Note that a given material particle $\mathbf{x}$ will remain in nucleation phase until there is another $\mathbf{x}'$ in horizon with a damage index $\phi(\mathbf{x}') \geq 0.5$ [30]. After particle $\mathbf{x}$ changes into growth phase, the parameters in Eq. (12) can be calculated by comparing with the Paris parameters $C$ and $M_2$, which can be experimentally obtained [31]. With a discretization of the cycle numbers the fatigue equation Eq. (12) in growth phase can be rewritten as

$$\begin{cases} \frac{\varphi_{x,x'}^{n}-\varphi_{x,x'}^{n-1}}{N(n)-N(n-1)} = -\gamma_2(\varepsilon)(\varepsilon_{x,x'}^{n})^{m_2} = -(n_2\varepsilon + c_2)(\varepsilon_{x,x'}^{n})^{m_2} \\ \varphi_{x,x'}^{0} = 1 \end{cases} \tag{18}$$

The backward finite difference discretization method is adopted here, where $\varepsilon_{x,x'}^{n}$ is cyclic strain of the bond between particles $\mathbf{x}$ and $\mathbf{x'}$. When the initial fatigue life $\varphi^{0}{}_{x,x'}$ of this bond is given, the fatigue life at any time step $\varphi_{x,x'}^{n}$ can be iteratively calculated after the parameters $n_2$, $c_2$ and $m_2$ are computed.

Induced by stress concentration, fatigue crack nucleates and grows into a macroscale crack. The crack growth rate can be determined by the Paris law, equating it to the work done in PD method, we have

$$\begin{cases} \frac{da}{dN}(N) = c\Delta K^{M_2} \\ \frac{da}{dN}(N) = \beta\gamma_2(\varepsilon)\varepsilon_{core}^{m_2} = \beta(n_2\varepsilon_{core} + c_2)\varepsilon_{core}^{m_2} \end{cases} \tag{19}$$

Because the stress intensity factor (SIF) is proportional to bond strain, cyclic change in SIF is proportional to bond strain amplitude, and thus we can set $m_2 + 1 = M_2$ here. Comparing the crack growth rate obtained by experiments with the PD results using any three pairs of arbitrary values $n'_{1,2,3}$, $c'_{1,2,3}$ and the already calibrated $m_2$, variables $n_2$, $c_2$ can be determined.

$$\begin{cases} n_2\varepsilon_{core} + c_2 = (n'_1\varepsilon_{core} + c'_1)\frac{da/dN}{(da/dN)'_1} = (n'_1\varepsilon_{core} + c'_1)\frac{c\Delta K^{M_2}}{(da/dN)'_1} \\ n_2\varepsilon_{core} + c_2 = (n'_2\varepsilon_{core} + c'_2)\frac{da/dN}{(da/dN)'_2} = (n'_2\varepsilon_{core} + c'_2)\frac{c\Delta K^{M_2}}{(da/dN)'_2} \\ n_2\varepsilon_{core} + c_2 = (n'_3\varepsilon_{core} + c'_3)\frac{da/dN}{(da/dN)'_3} = (n'_3\varepsilon_{core} + c'_3)\frac{c\Delta K^{M_2}}{(da/dN)'_3} \end{cases} \tag{20}$$

### 2.3. Reliability PD model for fatigue

Predicting the remaining fatigue life of structures under complex fatigue loading is a challenging task since the time to failure depends on a multitude of variables, many of which are stochastic in nature. The safety of a structure can never be completely guaranteed, if we only utilize deterministic methods. Therefore, it is necessary to carry out the fatigue study from the perspective of reliability, whereby the remaining life is calculated for a certain probability of failure and a given confidence interval.

Combining response surface method with PD fatigue method, a fatigue reliability PD (FRPD) model is proposed. The flow chart of the method is shown in Fig. 3, the specific steps of FRPD method are as follows:

(1) Approximate the reliability function as a quadratic polynomial with no cross terms.

$$\bar{G}(X_1, X_2, \cdots, X_n) = a + \sum_{i=1}^{n} b_i X_i + \sum_{i=1}^{n} c_i X_i^2 \tag{21}$$

where a, $b_i$, $c_i$ ($i = 1,2, \ldots, n$) are undetermined coefficients. A total of $(2n + 1)$ undetermined coefficients are involved;

(2) Take the initial point $P^{(k)} = P^{(1)} = (x_1^{(1)}, x_2^{(1)}, \ldots, x_{n+1}^{(1)})$ as the center point, where $k$ is the iteration number;
(3) Fit the expression of $\overline{G}(X_1, X_2, \ldots, X_n)$, select $(2n + 1)$ points $x^k{}_{(1)}$, $x^k{}_{(2)}$, …, $x^k{}_{(n+1)}$, and $2n$ points $x^k{}_{(1)}$, $x^k{}_{(2)}$, …, $x^k{}_{(i)} \pm f\sigma_i$,…, $x^k{}_{(n+1)}$ ($i = 1,2, \ldots, n$), where $\sigma_i$ is the standard deviation of the variable $X_i$. Coefficient $f$ adopts 2 or 3 at the 1st iteration, adopts 1 in other iterations. By using the PD fatigue life prediction method, these $(2n + 1)$ checkpoints can be calculated from the fatigue numerical test;
(4) The undetermined coefficients $a_i$, $b_i$, $c_i$ ($i = 1, 2, \ldots, n$) can then be obtained from the $(2n + 1)$ checkpoints adopted in step (3), the approximate reliability function $\overline{G}$ in this step can be calculated;
(5) Apply the JC method [32] to compute the checkpoint $P^{*(k)}$ and the reliability index $\beta^{(k)}$ in the approximate reliability function $\overline{G}$;
(6) Judge whether the convergence condition $|\beta^k\text{-}\beta^{k-1}|/\beta^k < \varepsilon_0$ is satisfied ($\varepsilon_0$ is the convergence precision). Stop the iteration immediately when the condition is satisfied, both the new design checkpoint $P^*$and the new reliability index $\beta = \beta^{(k)}$ can then be obtained. Otherwise, the interpolation method is used to obtain interpolation points.

$$P_M^{(k)} = P^{(k)} + (P^{*(k)} - P^{(k)})\frac{G(P^{(k)})}{G(P^{(k)}) - G(P^{*(k)})} \tag{22}$$

Compare $P^{(k)}{}_M$ and $P^{*(k)}$, select the point closer to the limit state surface as the new center point, and return to step (3) for the next iteration until the convergence condition is satisfied.

## 3. Numerical simulation and analysis

In this section, numerical simulations of fatigue crack growth are performed using the proposed PD method. The results obtained by fatigue tests, analytical methods and FEM are given for comparison. The simulations are implemented in a Fortran code, and Tecplot is utilized to visualize the results. Four cases are simulated with the first one using aluminum alloy AA2024-T351 [33] and

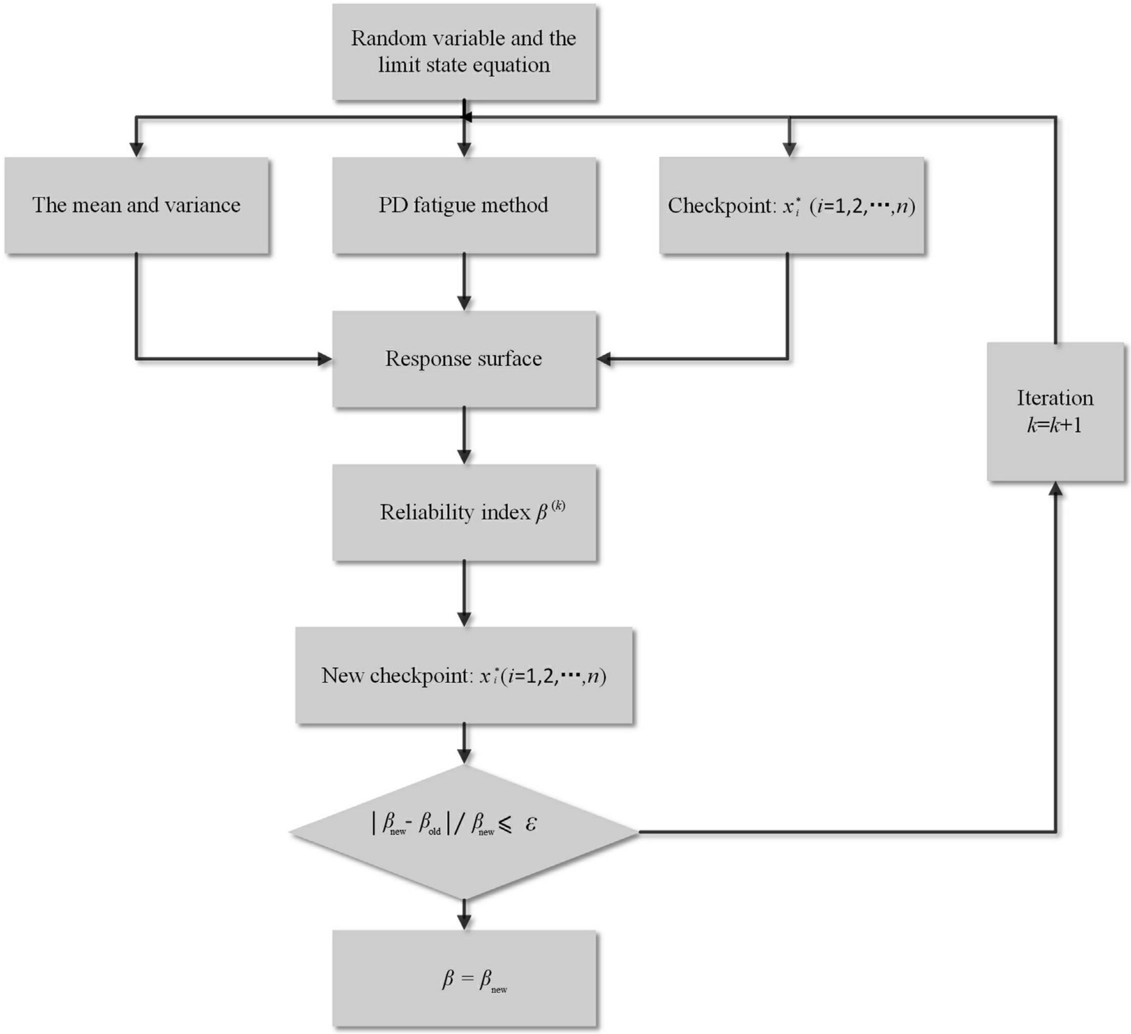


**Fig. 3.** Flow chart for FRPD analysis.

the next two using aluminum alloy 7075-T651 [31]. At the end of this section, the proposed method is used to calculate the fatigue failure probability of thin-walled members of the Ting Kau Bridge under actual vehicle loads. Note that since the lengths of all the specimens are much larger than the notch size, the square plate problem can be approximated as a central I-type crack infinite plate problem [34].

### 3.1. *Verification of fatigue crack path accuracy*

The expected crack path of aluminum alloy AA2024-T351 under biaxial fatigue loadings are first studied. The geometric configuration and loading condition are given in Fig. 4. The same problem was previously investigated in Breitbarth and Besel [33] where the experimental and FEM results are available. The present results obtained by using the PD method are compared to the results from Breitbarth and Besel [33].

A biaxiality ratio λ is utilized to characterize the biaxial stress condition in Eq. (23).

$$\lambda = \frac{\sigma_x}{\sigma_y} \tag{23}$$

where $\sigma_x$ and $\sigma_y$ represent the stress parallel and perpendicular to the initial notch, respectively. The properties of the material are presented in Table 1. The specimens are tested at the frequency of 5 Hz with loading ratio $\lambda = 3$, $\sigma_y = 40$ MPa and the phase difference $\Delta\varphi = 0$. The initial notch is aligned in the $x$ direction with a length of 80 mm. A small deviation is pre-set at both ends of the initial notch with an orientation of 45° and a center symmetric of 1.5 mm. The crack pattern will be completely axisymmetric (more precisely, a horizontal line) when the geometric dimensions and loadings are both axisymmetric, because a horizontal central crack can only develop along the horizontal direction under the condition of x-axis symmetry. This representative defect size is very

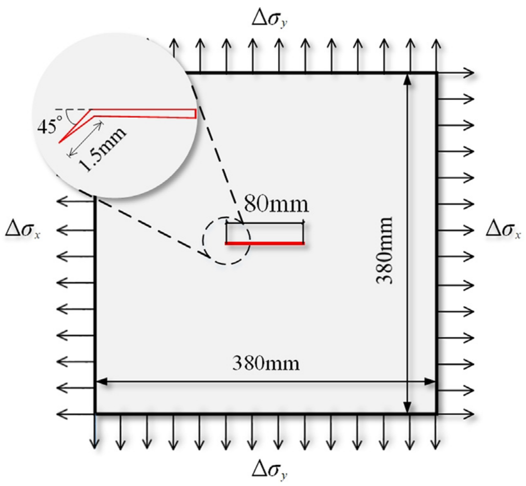


**Fig. 4.** Geometric configuration and loading condition.

**Table 1**
Material parameters [33].

| Parameters | $E$/(GPa) | $\rho/(kg/m^3)$ | $a_0$/(mm) | $C$ | $M$ |
|---|---|---|---|---|---|
| | 71 | 2,850 | 40 | $10^{-29}$ | 3 |

consistent with the selected 0.1 μs step size and the mesh size used in the study. Generally, very small geometric perturbations are also likely for true crack paths due to microscopic inhomogeneities or defects that exist along the path of the crack [35]. Note that all of the quasi-static simulations are conducted using the adaptive dynamic relaxation method.

Firstly, convergence study is conducted with attempt to determine whether the size of the nonlocal region is sufficiently small to obtain a crack path that no longer changes when the horizon size decreases further. In the PD model, the two numerical convergence standards are $m$-convergence and $\delta$-convergence. In this subsection, $\delta$-convergence is achieved through crack paths. We perform the test for $m = \delta/\Delta x = 4$ and use the following values for the horizon size: 8, 4, and 2 mm. Each horizon size determines the grid spacing used with it because $m$ is fixed; therefore, the corresponding $\Delta x$ values are 2, 1, and 0.5 mm, respectively. The crack path for the three cases are shown in Fig. 5. It is found that as the horizon decreases, the fatigue crack path does not substantially change but becomes more defined, which is consistent with the assertion that the spread of damage is related to the horizon size. The grid spacing value $\Delta x = 0.5$ mm provides a good balance between accuracy and efficiency, and thus the same $\Delta x$ is utilized for the rest computations in this study.

The fatigue crack patterns of the present simulations and experiments in [33] are compared in Fig. 6. Fig. 6**(a)** exemplarily shows the gauge area of AA2024-T351 specimen with the kinked crack after the fatigue test. Fig. 6**(b)** gives the equivalent crack path obtained by the PD method. It can be seen from figure that there is a higher damage index near the crack path (blue to red). The slope of two stable crack paths are both 85 degree which are affected by biaxiality ratio ($\lambda = 3$). Due to the artificial small deviation, the stress concentrated at the left side of the crack tip, which leads to a higher failure rate on the left side of the fatigue crack than on the right side, thus forming a slight “s” shape but still has good consistency with the experimental results. Changing the biaxiality ratio has a significant effect on the fatigue crack extension angle. More biaxial fatigue cases are simulated to investigate the fatigue crack growth behavior in detail, and the results simulated by PD method and FEM [33] are compared in Fig. 7. It is observed from Fig. 7 that the resultant crack path obtained by the two different methods are very close under different biaxial fatigue loadings. The cracks grow in a stable pattern, under a biaxiality ratio of $\lambda = 1$ the crack grows almost straight with slope angle less than 1 degree. When $\lambda = 1.5$, the PD simulation predicts an angle of about 45° for the stable crack propagation direction, which is in fairly good agreement with the FEM results. With the increase of $\lambda$ and a same value of vertical fatigue loading, the slope increases to 75 degree ($\lambda = 2.5$) and 85 degree ($\lambda = 3$). In spite of the limitation of the database, the consistency of the research results distinctly proves that with different biaxiality ratios, the crack paths in AA2024-T351 aluminum alloys can be sufficiently predicted with the proposed method.

The effect of initial notch angle on the fatigue performance is further analyzed. Fig. 8 shows the crack paths of numerical samples with different initial notch angles ($\theta = 0°, 30°, 60°$and 90°) and biaxiality ratios ($\lambda = 1.2, 1.56, 2.5, 3$). Although the cycle number in Fig. 8 looks impractically huge, all the simulations have the same cycles when stress redistribution does not occur, which can greatly reduce the simulation time. The accuracy of the proposed method has been verified by comparing the PD results with the experiment from Breitbarth and Besel [33]. Moreover, since this example focused on the effect of initial notch angle and biaxiality ratio $\lambda$, there is no need to verify this example by experiment again. It’s obvious in Fig. 8 that, with a fixed angle the crack is more likely to propagate in the horizontal direction when $\lambda$ increases, and crack inclination angle increases simultaneously. When crack inclination angle is less than 45°, the fatigue life of the specimen under high $\lambda$ is longer than that under low $\lambda$, and the opposite phenomena occur when

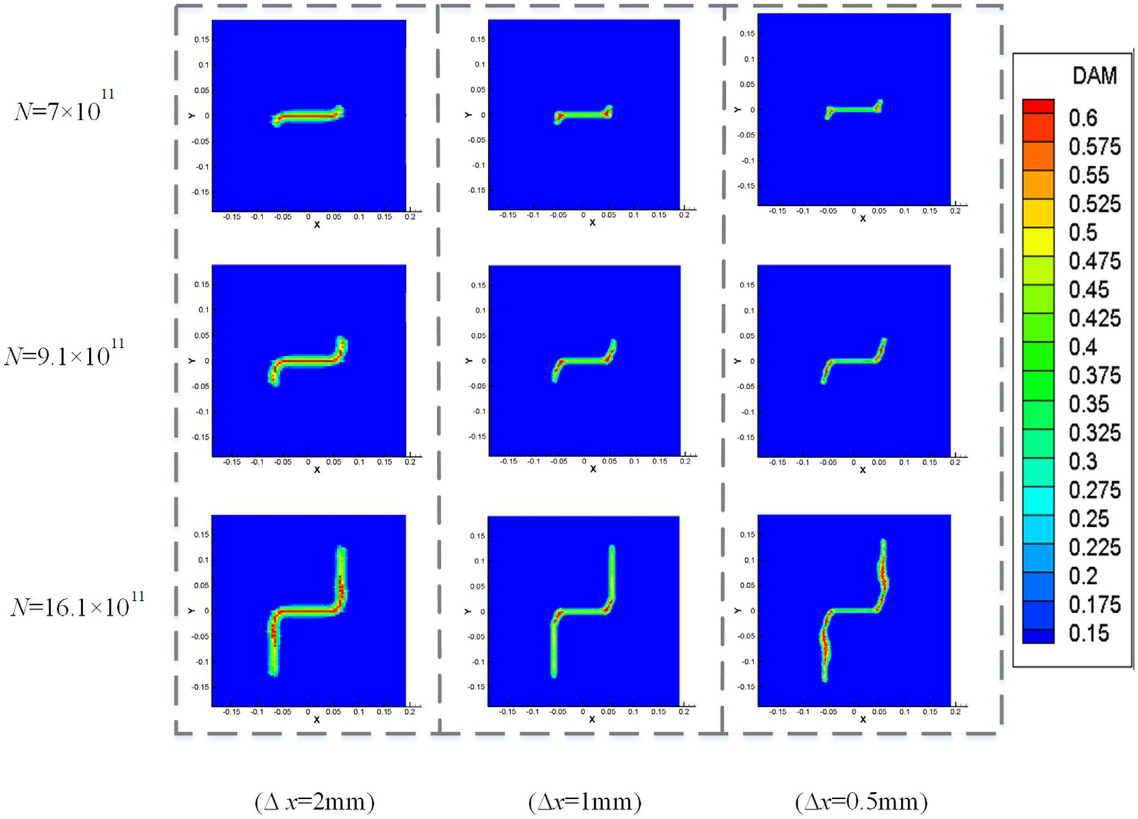


**Fig. 5.** $\delta$-Convergence in terms of fatigue crack path computed with different grid spacing.

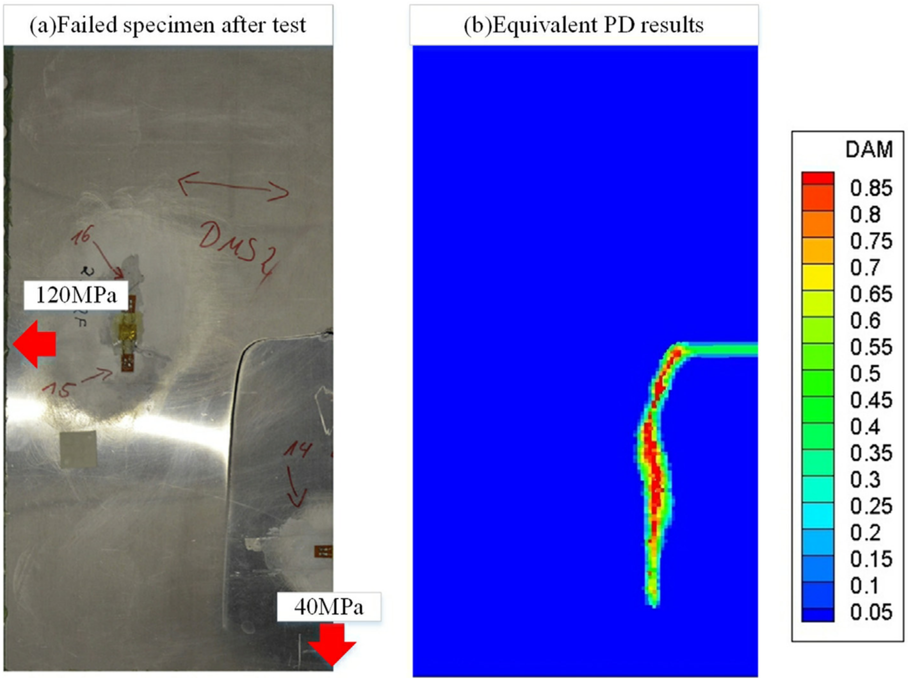


**Fig. 6.** (a) AA2024-T351 specimen after test with initial notch; (b) PD analysis showing equivalent damage pattern after failure.

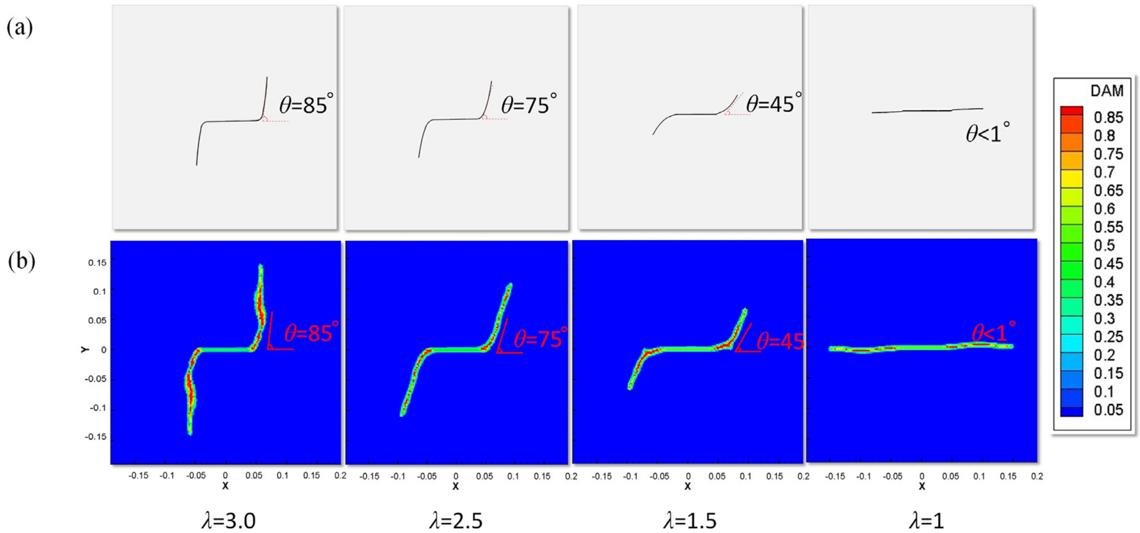


**Fig. 7.** Simulated crack paths of biaxial tests: (a) FEM results; (b) PD results.

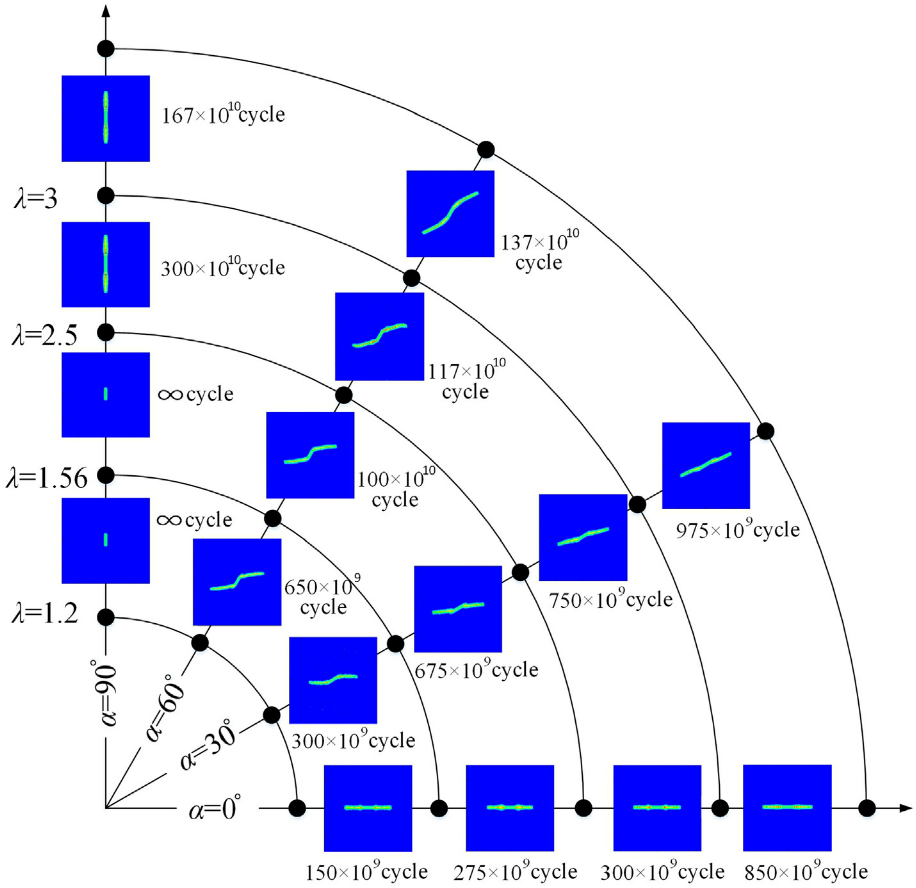


**Fig. 8.** Rules of single crack propagation, curving and branching in the numerical specimens subjected to biaxial fatigue loading.

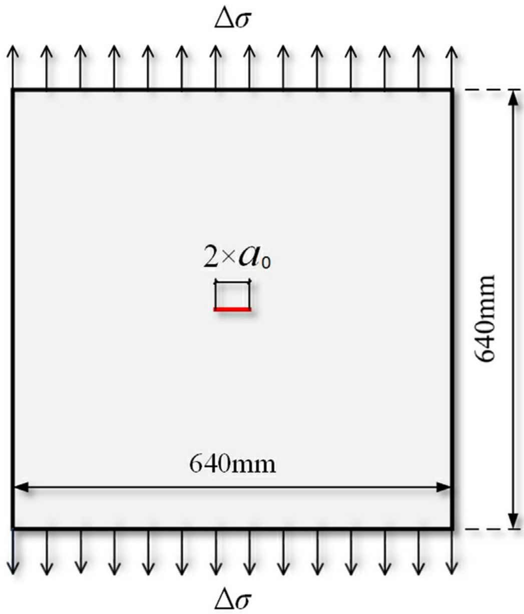


**Fig. 9.** A square plate with a center crack subjected cyclic tensile loading.

the initial angle is greater than 45°, which are consistent with Duan et al.'s conclusion [36].

### 3.2. Verification of fatigue life accuracy

In this case, a central-crack thin rectangular plate of dimensions 640 mm × 640 mm (see Fig. 9), which is subjected to acyclic loading with constant amplitude $\Delta\sigma = 100$ MPa, the stress ratio $R = \Delta\sigma_{\min}/\Delta\sigma_{\max} = 0$, is considered. The initial notch is pre-set at the center of the specimen in the horizon direction, $\alpha = 0°$. The accuracy of the proposed method for solving fatigue life is verified by comparing the PD results with the analytical solutions. The material parameters of the specimen are given in Table 2. Based on the proposed expressions, the PD parameters $n_1$, $c_1$, $m_1$ and $n_2$, $c_2$, $m_2$ are calculated, as summarized in Table 3. Half of the initial notch is taken as $a_0 = 10$ mm, refer to Zhao and Jiang's work [31] for more details about the experiment. Note that the static analysis is the basis of PD fatigue simulation and the most time-consuming part. A multi-grid method [37] is adopted to improve the calculation efficiency.

(1) Analytical solution

Analytical fatigue life is calculated to verify the accuracy of the proposed PD method. The specimen size has been described in detail as shown in Fig. 9. The resulting SIF amplitude around the initial crack tip is

$$\Delta K = \sqrt{\frac{\Delta J \cdot E}{(1-\nu^2)}} = \sqrt{\frac{4082\,\mathrm{Pa}\cdot m \times 70\,\mathrm{GPa}}{1-0.09}} = 17.72\,\mathrm{MPa}\sqrt{m} \tag{24}$$

Here, $J$ represents the $J$-integral as a path-independent integral in elastoplastic fracture mechanics which is used to describe the stress situation of a crack tip region. The selection of $J$-integral range was based on the crack size, that is, a 5 mm × 5 mm square was selected and the crack tip was kept at the center. Refer to the research of Hu et al. [29] for more details. The Poisson's ratio of aluminum alloy $\nu$ is approximately 0.3 according to Zhao and Jiang's work [31]. The SIF amplitude $\Delta K$ greater than 1 MPa·m$^{1/2}$ at the initial crack tip indicates that the fatigue crack will propagate.

The critical crack size $a_c$ is calculated by fracture mechanics as

$$a_c = \frac{1}{\pi}\left(\frac{K_{\mathrm{Ic}}}{\sigma_{\max}}\right)^2 = 79.56\,\mathrm{mm} \tag{25}$$

**Table 2**
Material parameters [31].

| Parameters | $E$/(GPa) | ρ/($kg/m^3$) | $a_0$/(mm) | $K_{\mathrm{Ic}}$(MPa·m$^{1/2}$) | $C$ | $M_1$ | $M_2$ |
|---|---|---|---|---|---|---|---|
| | 70 | 2,850 | 10 | 50 | $10^{-29}$ | 3.4 | 3 |

**Table 3**
Parameters used in the PD model.

| Parameters | $n_1$ | $c_1$ | $n_2$ | $c_2$ | $m_1$ | $m_2$ |
|---|---|---|---|---|---|---|
| | 2,100 | 4.2 | 1,800 | 3.6 | 2.4 | 2 |

Here, $K_{Ic}$ represents the critical SIF. The value of $K_{Ic}$ and the parameters in Paris' law can be found in Table 2. By using the Paris' law, the fatigue life can be calculated as

$$N = \int_{a_0}^{a_c} \frac{da}{C(\Delta K)^{M_2}} = \frac{1}{C(M_2/2-1)(\Delta\sigma\sqrt{\pi})^{M_2}}\left(\frac{1}{a_0^{M_2/2-1}} - \frac{1}{a_c^{M_2/2-1}}\right) = 2.9\times 10^4\,\text{cycle} \tag{26}$$

(2) PD fatigue method

The fatigue life is calculated by using the proposed PD fatigue method. The same material parameters as the analytical method are used, while the iterative time step $dt$ is taken as $10^{-7}$s.

The critical crack size $a_c$ (the crack length when non-fatigue damage occurs) calculated by the PD fatigue method is 83 mm, as shown in Fig. 10. The PD calculation results and the analytical solutions are compared in Table 4. It is found that the fatigue life $N_p$ obtained by the two methods are quite consistent, while the critical crack size $a_c$ shows a certain deviation. In fact, the deviation increases with the crack growth, as shown in Fig. 11. The inevitable deviation is produced by the infinite plane simplification. However, when the crack propagates into the final stage along with the crack length close to the critical size, the corresponding number of alternating load cycles contributes little to the fatigue life. Thus, the critical crack size predicted by the PD method is reasonably acceptable.

### 3.3. Verification of fatigue reliability accuracy

A specimen subjected to cyclic tensile loadings, as shown in Fig. 12**,** is analyzed to verify the accuracy of the proposed FRPD method. The random parameters and their distribution functions given in Table 5 were selected based on the statistical characteristics of these data: (1) Fracture toughness $K_{Ic}$: suggested by Wallin K [38], $K_{Ic}$ follows a normal distribution, the range of average value is 44–220 MPa·m$^{1/2}$, and the coefficient of variation should be within the range of 0.15–0.25; (2) Crack length $a$: as suggested in Bullough et al. [39] the crack size follows a log-normal distribution, and it was recommended that the coefficient of variation ranges from 0.1 to 0.5; (3) External load $\sigma$: Riahi et al.'s [40] research suggested that $\sigma$ follows a log-normal distribution and the coefficient of variation ranges from 0.1 to 0.3; (4) Other random parameters: Liu [41] suggested that when there is a lack of statistical data, it can be conservatively assumed that the parameters follow a normal distribution, and their means and coefficients of variation can be determined based on experience. Note that in this case, two identical symmetric circular holes ($h$ = 20 mm, $R$ = 10 mm) are pre-set according to Newman's paper [42], for the purpose of calculating the SIF with the stress shielding effect included. In fracture mechanics, the dimensionless SIF of the I-type crack is given as

$$F_I = \frac{K_I}{\sigma\sqrt{\pi a}} \tag{27}$$

In PD method, the SIF is derived by calculating $J$-integration. Interested readers are referred to Panchadhara and Gordon [43] for specific details.

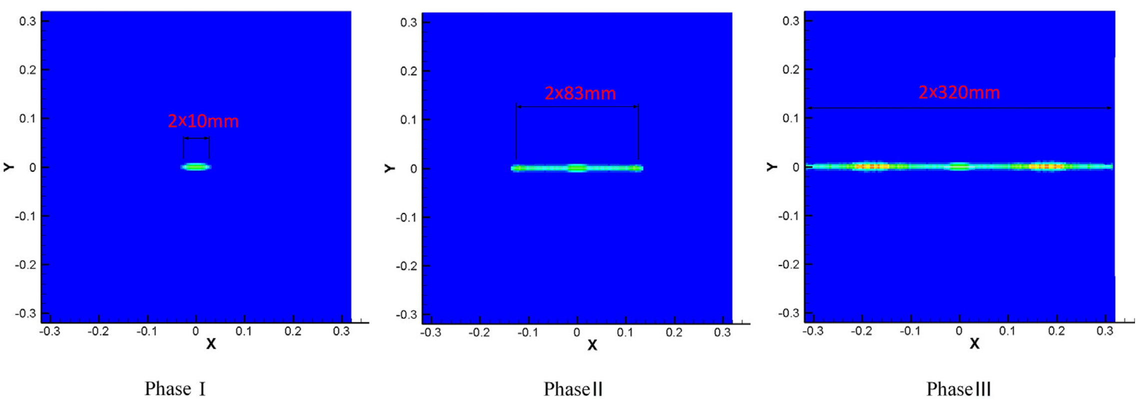


**Fig. 10.** Three phases of fatigue fracture: (a) Phase I: the fatigue crack initiation phase; (b) Phase II: the fatigue crack growth phase; (c) Phase III: the fatigue failure phase.

**Table 4**
Comparison of results between the two methods.

| Methods | $a_c$/(mm) | $N_P$/(cycle) |
|---|---|---|
| PD | 83 | $2.92 \times 10^4$ |
| Analytical solution | 79.56 | $2.9 \times 10^4$ |

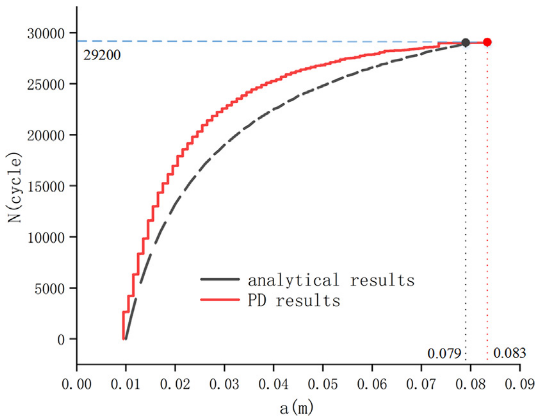


**Fig. 11.** Number of cycles versus the crack size.

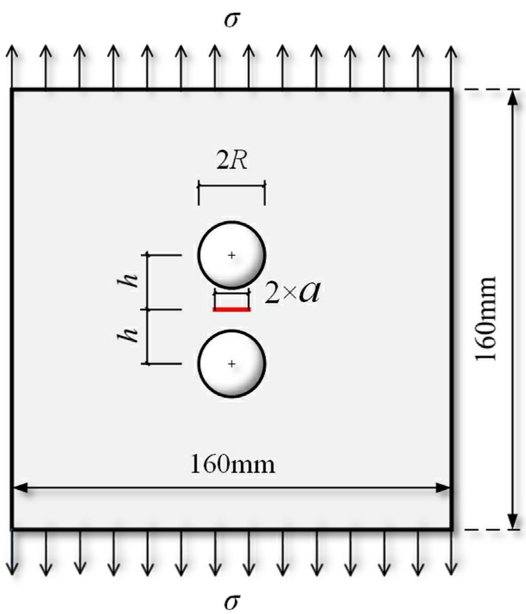


**Fig. 12.** Square specimen with initial notch between two holes.

**Table 5**
The statistical characteristics of random variables.

| Random Variables | Means | Coefficient of Variation | Distribution Type |
|---|---|---|---|
| $K_{Ic}$ | 50 MPa·m$^{1/2}$ | 0.2 | Normal distribution |
| $\nu$ | 0.3 | 0.05 | Normal distribution |
| $a$ | 10 mm | 0.2 | Lognormal distribution |
| $\sigma$ | 200 MPa | 0.1 | Lognormal distribution |
| $C$ | $10^{-29}$ | 0.2 | Lognormal distribution |
| $M_1$ | 3.4 | 0 | Constant |
| $M_2$ | 3 | 3 | Constant |

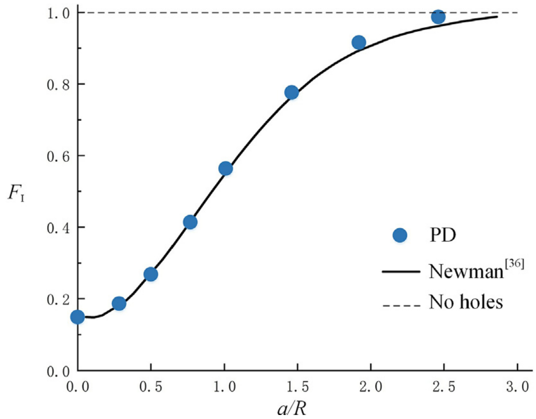


**Fig. 13.** Values of $F_I$ corresponding to different crack sizes.

Accurately calculating $F_I$ (not a necessary part in PD calculation) is one of the indicators to assess the reliability of the proposed method. In PD theory, fatigue cracks extend spontaneously without additional fracture criteria, so the calculations under different fracture modes have no difference. Therefore, only the fatigue reliability accuracy of the model under mode I condition was validated. The $F_I$ values obtained by the PD solution were compared with Newman's results in Fig. 13. It is seen from Fig. 13 that the present results are quite consistent with Newman's results. In addition, $F_I$ increases significantly with the growth of $a/R$; When $a/R$ is greater than 3.0, the value of $F_I$ is infinitely approaching to the dash line, which represents the SIF calculated with no holes. It illustrates that when the crack size is more than 3 times of the circular hole diameter, the shielding effect on the crack tip can be neglected.

The FRPD method proposed in this paper is utilized to analyze the fracture reliability of a pre-notched square plate with no holes and is also compared with the direct Monte Carlo method. In the reliability function Eq. (21), the random variables include material fracture toughness $K_{Ic}$, Poisson's ratio$\nu$, crack size $a$, tensile stress $\sigma$ and Paris parameters $C$, $M_2$. These parameters are independent of each other and their statistical characteristics are summarized in Table 5. The calculation results in each iterative step are listed in Table 6, where the convergence accuracy is set as $\varepsilon = |\beta^k\text{-}\beta^k\text{-}1| = 0.001$.

It is seen from Table 6 that the FRPD method only needs a small number of iterations to obtain a convergent result. The calculation results of the proposed method are in good agreement with the direct Monte Carlo results ($P_{MCf} = 0.06\%$, the relative error is about 2.8%). In terms of computational time, the proposed PD method only needs 33 times of numerical calculations ($7.37 \times 10^4$ s, about 1/21 of direct Monte Carlo method), which is a great calculation efficiency improvement when performing fatigue reliability calculations.

Finally, the influence of stress magnitude on the fatigue failure probability is discussed. The PD results and the analytical solutions as the mean cyclic tensile stress $E(\sigma)$ increases from 100 MPa to 300 MPa are compared in Fig. 14. It is not hard to find that the reliability index $\beta$ decreases with the increasing $E(\sigma)$. When the tensile stress $E(\sigma)$ increases gradually, the failure probabilities obtained by the FRPD method are in good agreement with the analytical solutions. However, the FRPD results have some errors with the analytical solution, but the errors are acceptable because the analytical solution is based on infinite assumptions while the specimen calculated by the FRPD method has to be finite.

### 3.4. Fatigue reliability of Ting Kau bridge

In the fourth case, the Ting Kau Bridge is taken as an example to apply the FRPD method in order to evaluate the fatigue performance of the bridge under actual vehicle loads and also to calculate the fatigue reliability index of thin-walled members in the bridge.

**Table 6**
Iterations for Case with no holes.

| Random Variables | Checkpoints | | |
|---|---|---|---|
| | First Iteration $\beta^{(1)} = 2.067$ | Second Iteration $\beta^{(2)} = 2.071$ | Third Iteration $\beta^{(3)} = 2.00709$ |
| $K_{Ic}$ | 34.72 MPa·m$^{1/2}$ | 34.91 MPa·m$^{1/2}$ | 34.8 MPa·m$^{1/2}$ |
| $\nu$ | 0.3 | 0.3 | 0.3 |
| $a$ | 0.98 mm | 1.14 mm | 1.106 mm |
| $\sigma$ | 199 MPa | 214.37 MPa | 219.18 MPa |
| $C$ | $0.96 \times 10^{-29}$ | $1.1 \times 10^{-29}$ | $1.1 \times 10^{-29}$ |
| $m_1$ | 2.4 | 2.4 | 2.4 |
| $m_2$ | 2 | 2 | 2 |

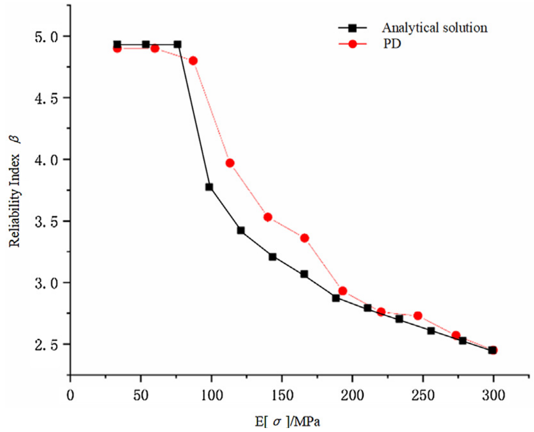


**Fig. 14.** Reliability index change with different stress magnitude mean value $E(\sigma)$.

The three-dimensional FE model of the entire Ting Kau Bridge was established using the finite element software ANSYS. The model contains a total of 12,688 nodes and 72,968 elements, including 14,929 beam elements, 25,720 shell elements, 26,042 solid elements, and 6227 contact elements. According to the natural frequencies and modal shapes obtained by the health monitoring system installed on the bridge, the FE model was modified to make it more in line with the actual situation. For detailed information about the three-dimensional finite element model of Ting Kau Bridge, please refer to the related special report [44].

According to the measured traffic information, the fatigue stress spectrum of the steel stringer and steel girder can be established. The traffic information of the Ting Kau Bridge is collected and recorded by the weigh-in-motion (WIM) system installed at the Tsing Yi shore abutment. It mainly includes information of the vehicles' number and weight, which passing through various lanes of the bridge, refer to the research report of Ting Kau Bridge [44] for specific details. It is seen from the schematic diagram of the Ting Kau Bridge shown in Fig. 15 that key fatigue members can be selected from the steel stringers on the axes 1000, 2000, 3000, 4000 and the steel girders on the east and west side of bridges [45]. Since the WIM system is not installed on the shoulder and only a very small number of vehicles are considered to occupy the shoulder, the fatigue damage caused by the vehicle on the shoulder can be ignored.

The special vehicle load spectrum is further converted into standard fatigue vehicle (SFV) load spectrum [46] as shown in Table 7. The stress-affected line shape of the steel stringer and the steel girder of the Ting Kau Bridge deck have basically only one distinct peak, it can be approximated that the entire stress history contains only one stress cycle. Since the vehicle wheelbase is much smaller than the bridge span, this simplification of the fatigue load spectrum is acceptable. Then, the maximum and minimum stresses of the components caused by an $i$-group vehicle passing through the $j$th lane can be calculated by using conversion factor $k_{\mathrm{w},i}$ as

$$\left.\begin{aligned}\sigma_{\mathrm{RV,max},ji} &= k_{\mathrm{w},i}\sigma_{\mathrm{SFV,max},j}\\ \sigma_{\mathrm{RV,min},ji} &= k_{\mathrm{w},i}\sigma_{\mathrm{SFV,min},j}\end{aligned}\right\}(i = 1, 2, \cdots, n_{\mathrm{T}};\ j = 1, 2, \cdots, n_{\mathrm{L}}) \tag{28}$$

where $n_{\mathrm{T}}$ is the total number of vehicle groups; $n_{\mathrm{L}}$ is the total number of traffic lanes. Since the stress caused by the dead load is usually very large, the influence of the dead load should also be considered in the stress amplitude calculation. Therefore, rewrite Eq. (28) as

$$\left.\begin{aligned}\sigma_{\mathrm{RV,max},ji} &= k_{\mathrm{w},i}\sigma_{\mathrm{SFV,max},j} + \sigma_{DL}\\ \sigma_{\mathrm{RV,min},ji} &= k_{\mathrm{w},i}\sigma_{\mathrm{SFV,min},j} + \sigma_{DL}\end{aligned}\right\}(i = 1, 2, \cdots, n_{\mathrm{T}};\ j = 1, 2, \cdots, n_{\mathrm{L}}) \tag{29}$$

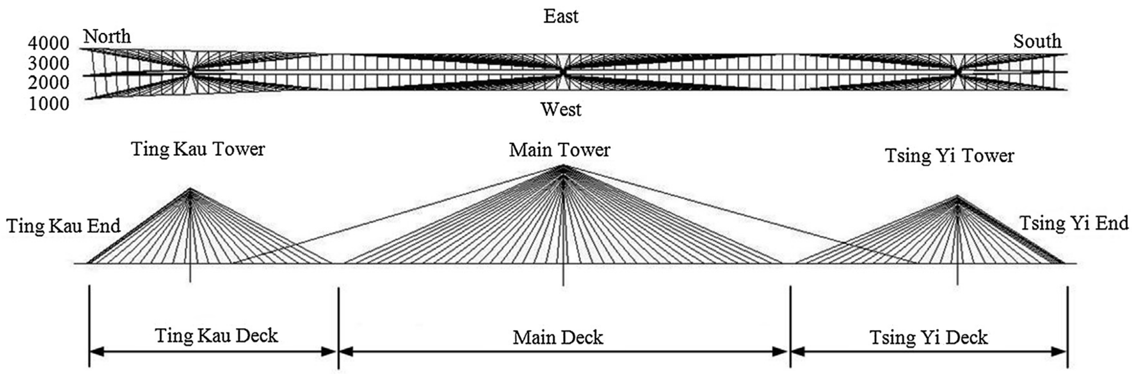


**Fig. 15.** Plan and elevation of the Ting Kau Bridge [44].

**Table 7**
Annual SFV spectrum of the Ting Kau Bridge (2007) [44].

| Number | Ratio to SFV ($k_w$) | Number of vehicles heading to Ting Kau (Westbound) | | | Number of vehicles heading to Tsing Yi (Eastbound) | | |
|---|---|---|---|---|---|---|---|
| | | Slow lane | Mid Lane | Fast lane | Slow lane | Mid Lane | Fast Lane |
| 1 | 0.094 | 2,032,838 | 4,689,433 | 3,059,542 | 3,412,120 | 4,100,825 | 2,457,824 |
| 2 | 0.313 | 1,411,792 | 1,229,028 | 154,470 | 130,751 | 945,198 | 671,598 |
| 3 | 0.688 | 1,133,915 | 577,046 | 3385 | 985 | 385,923 | 1,355,270 |
| 4 | 1.063 | 262,855 | 79,024 | 975 | 157 | 61,135 | 346,937 |
| 5 | 1.438 | 78,618 | 12,866 | 207 | 32 | 20,347 | 124,463 |
| 6 | 1.813 | 23,313 | 502 | 46 | 2 | 2,460 | 42,313 |
| 7 | 2.188 | 3,774 | 5 | 2 | 0 | 325 | 6,663 |
| 8 | 2.438 | 571 | 0 | 1 | 0 | 391 | 1,599 |
| Sum | | 4,947,676 | 6,587,904 | 3,218,628 | 3,544,047 | 5,516,604 | 5,006,667 |

where $\sigma_{DL}$ is the stress of the key component under dead load. In addition, the influence of the compressive stress should be ignored when calculating the stress amplitude, because the compressive stress cannot cause crack propagation in the steel structures [47]. Therefore, the key component stress amplitude caused by an $i$th group vehicle passing through the $j$th lane can be expressed in Eq. (30).

$$\Delta\sigma_{RV,ji} = \begin{cases} \sigma_{RV,max,ji} - \sigma_{RV,min,ji} & \sigma_{RV,min,ji} \geqslant 0 \\ \sigma_{RV,max,ji} & \sigma_{RV,min,ji} < 0 \\ 0 & \sigma_{RV,max,ji} < 0 \end{cases} \quad (i = 1, 2, \cdots, n_T;\ j = 1, 2, \cdots, n_L) \tag{30}$$

In Eq. (30), $\Delta\sigma_{RV,ji} = 0$ means that the key component is under pressure and fatigue damage will not occur. Taking an SFV crossing the mid lane as an example, the stress history of the lower flange is plotted in Fig. 16. As shown in Fig. 16, since only one stress cycle is caused both in the steel stringers and the steel girders when each vehicle passes through the bridge, the cycle number of the stress is the same as the number of vehicles in the $i$th group, $j$th lane.

By comparing the maximum stress amplitude of the components caused by SFV (considering the dead load effect) [45], the key fatigue components of the Ting Kau Bridge can be determined and are summarized in Table 8. The detailed fatigue performance of the steel stringer and steel girders can then be analyzed by establishing a PD fatigue model. Since only the tensile stress can promote crack propagation, it is assumed that the initial notch appears on the lower flanges. Both central cracks and side cracks will be considered for steel stringers, while only the side cracks need to be considered for steel girders [48]. Note that all the cracks are considered to be penetrable.

The steel stringers and steel girders are thin-walled members, and the lower flange mainly bears the tensile stress inside the plate. In addition, considering that the initial notch is generally very small, and that the crack tends to expand in a direction perpendicular to the applied tensile load, the influence of the initial notch angle on the crack propagation can be ignored. Therefore, the crack propagation in steel stringers can be simplified as central I-type crack problem and unilateral I-type crack problem, while the crack propagation in steel girder can be simplified only as unilateral I-type crack problem, as shown in Fig. 17.

For the fatigue reliability analysis of the Ting Kau Bridge, consider these random variables: initial notch length $a_0$, material fracture toughness $K_{Ic}$, parameters in PD model $n$, $c$, m, SIF threshold $\Delta K_{th}$, multi-vehicle effect coefficient $K_F$, critical fatigue damage $D_c$, and the number of load spectrum vehicles $n_{ij}$ (total $n_L \times n_T$). Referring to [49], the fatigue life $L$ of steel stringers and steel girders can be expressed as

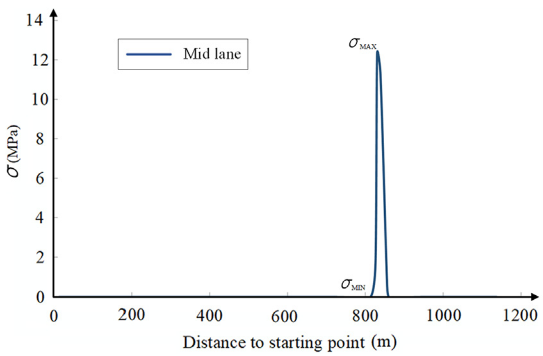


**Fig. 16.** Stress history of the steel cross girder lower flange due to SFV passing through Mid lane.

**Table 8**
Stress ranges of the critical components for fatigue failure [45].

| Component type | Component number | Maximum stress amplitude (MPa) | Component location |
|---|---|---|---|
| Steel Stringer | E33950 | 17.77 | Axis 1000, 303.3 m from the starting point |
| | E34506 | 17.16 | Axis 1000, 847.3 m from the starting point |
| | E33953 | 11.77 | Axis 2000, 303.3 m from the starting point |
| | E34521 | 12.19 | Axis 2000, 857.8 m from the starting point |
| | E35156 | 11.55 | Axis 3000, 303.3 m from the starting point |
| | E35725 | 11.99 | Axis 3000, 857.8 m from the starting point |
| | E35159 | 17.46 | Axis 4000, 303.3 m from the starting point |
| | E35728 | 17.11 | Axis 4000, 857.8 m from the starting point |
| Steel Girder | E29983 | 14.42 | west side of the bridge, 857.8 m from the starting point |
| | E30256 | 14.44 | west side of the bridge, 1033.3 m from the starting point |
| | E33090 | 15.16 | west side of the bridge, 857.8 m from the starting point |
| | E33402 | 14.81 | west side of the bridge, 1033.3 m from the starting point |

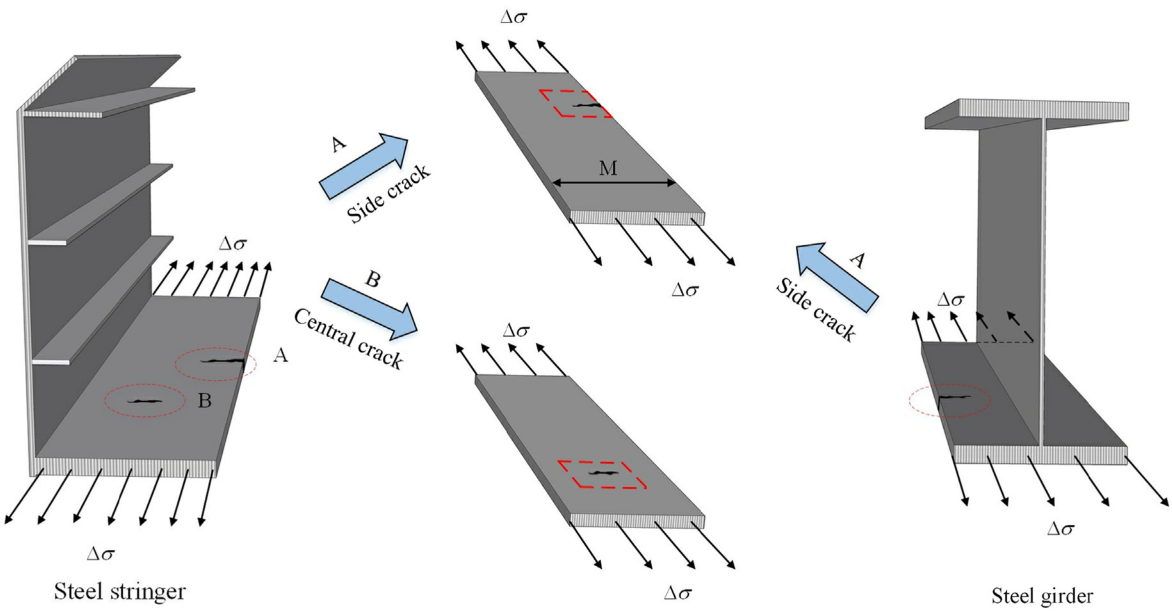


**Fig. 17.** Simplified model for PD fatigue analysis.

$$L(a_0, K_{Ic}, c_1, n_1, m_1, c_2, n_2, m_2, \Delta K_{th}, K_F, D_c, n_{11}, n_{12}, \cdots, n_{nL}, n_{nT}) = \frac{D_c}{K_F \sum_{j=1}^{n_L} \sum_{i=1}^{n_T} \left(\frac{\Delta\sigma_{RV,ij}}{\Delta\sigma_{th,0}(a_0, \Delta K_{th})}\right)^{2b} \frac{n_{ji}}{N_{RV,ji}(a_0, K_{Ic}, c_1, n_1, m_1, c_2, n_2, m_2)}} \quad (31)$$

where

**Table 9**
The statistical characteristics of random variables [49].

| Random variables | Mean | Coefficient of variation | Distribution type |
|---|---|---|---|
| $a_0$ | 10 mm | 0.2 | Lognormal |
| $K_{Ic}$ | 51 MPa·m$^{1/2}$ | 0.2 | Normal |
| $C$ | $6.94 \times 10^{-11}$m/cycle/(MPa $\times$ m$^{1/2}$)$^m$ | 0.2 | Lognormal |
| $\Delta K_{th}$ | 5.38 MPa·m$^{1/2}$ | 0.2 | Normal |
| $K_F$ | 1.5 | 0.2 | Normal |
| $D_c$ | 1.0 | 0.3 | Lognormal |
| $n_{ji}$ | Refer to [49] | 0.1 | Normal |

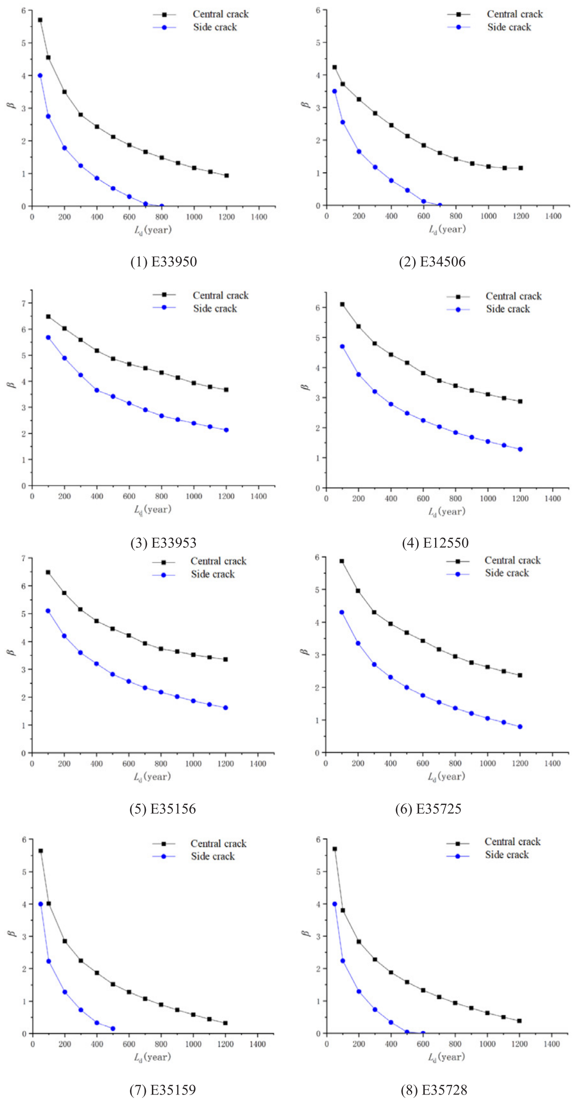


(1) E33950 (2) E34506

(3) E33953 (4) E12550

(5) E35156 (6) E35725

(7) E35159 (8) E35728

**Fig. 18.** Reliability index $\beta$ with different design fatigue life $L_d$ of: (1)–(8) Steel stringers; (9)–(12) Steel girders.

$$b = \begin{cases} 0 & \Delta\sigma_i > \Delta\sigma_{th,0} \\ 1 & \Delta\sigma_i \leqslant \Delta\sigma_{th,0} \end{cases}$$

$$N_{RV,ji} = \begin{cases} N_{RV,ji}(a_0,\ K_{Ic},\ c_1,\ n_1,\ m_1,\ c_2,\ n_2,\ m_2) & \Delta\sigma_i > \Delta\sigma_{th,0} \\ 10^7 & \Delta\sigma_i \leqslant \Delta\sigma_{th,0} \end{cases} \tag{32}$$

where $N_{\mathrm{RV},ji}(a_0,K_{\mathrm{Ic}},c_1,n_1,m_1,c_2,n_2,m_2)$ represents the fatigue life of the key components which can be calculated by the PD fatigue method, and the mean value and standard deviation of the fatigue life can be calculated by using the reliability method introduced in Section 2.3. Firstly, the fatigue life $L$ is fitted into a response surface function. Then the variables are randomly sampled as listed in Table 9. Finally, the relationship between the reliability index $\beta$ of all key components and the bridge design fatigue life $L_\mathrm{d}$ are determined respectively, as shown in Fig. 18 (1)–(12).

It is seen from Fig. 18 that for the same design fatigue life, the reliability index of the steel stringers under the condition of unilateral crack is significantly lower than those under the condition of the central crack, indicating that the unilateral crack is more prone to fatigue damage. For fatigue performance evaluation, the higher the target reliability index, the shorter the safe service life of the structure, and the higher the testing and maintenance costs required. In order to strike a balance between safety and economy, many scholars have studied the fatigue reliability index of steel bridges. The European Steel Structure Association recommends a target fatigue reliability index of 3.5 for all steel bridges. Therefore, in this case when the target reliability index $\beta = 3.5$, the design fatigue life of all key components is obtained from Fig. 18, which are summarized in Table 10.

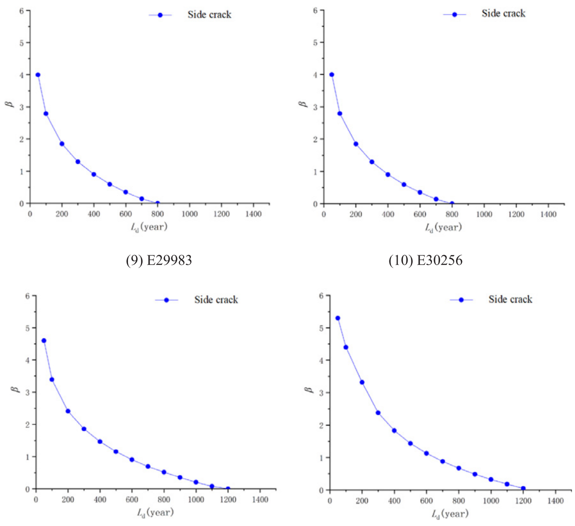


(9) E29983 (10) E30256

(11) E33090 (12) E33402

**Fig. 18.** (*continued*)

**Table 10**
Design fatigue life under target reliability index $\beta = 3.5$.

| Component type | Component number | Fatigue design life $L_d$ (year) | |
|---|---|---|---|
| | | Central Crack | Side Crack |
| Steel Stringer | E33950 | 203 | 65 |
| | E34506 | 153 | 49 |
| | E33953 | 1200 | 460 |
| | E34521 | 734 | 241 |
| | E35156 | 1033 | 325 |
| | E35725 | 580 | 175 |
| | E35159 | 146 | 68 |
| | E35728 | 130 | 62 |
| Steel Girder | E29983 | — | 68 |
| | E30256 | — | 68 |
| | E33090 | — | 90 |
| | E33402 | — | 187 |

## 4. Conclusions and future work

In the present study, a fatigue reliability model based on the PD theory was proposed aiming at capturing the fatigue crack growth and predicting the fatigue life of steel bridge components under repeated vehicle loading. The accuracy of the proposed fatigue model was verified by comparing the predicted results with both experimental and FEM simulation results. An example with three fatigue phases in modeling the fatigue cracking in a pre-notched steel plate under cyclic loadings was adopted for the purpose of illustration. It is found that the model can effectively simulate the whole process of fatigue damage evolution and the fracture process of the steel specimen. Based on the results from this study, the following conclusions can be drawn:

(1) The proposed PD fatigue method can effectively reproduce the fatigue crack growth patterns observed in experiments and is therefore able to offer convergent numerical simulations. For biaxial fatigue specimens with different biaxiality ratio λ, the crack patterns in aluminum alloy was well simulated by the proposed method. The crack patterns with different biaxiality ratios predicted by the proposed method were very consistent with the experimental and FEM results. Moreover, the fatigue life of the specimen obtained by the proposed method was very close to the analytical results.
(2) One main advantage of the proposed method lies in the significant reduction of computational time while retaining high accuracy. Due to the adoption of the response surface method and multi-grid method, the computation time of the FRPD method proposed in this study is approximately 1/21 of the time using the traditional Monte Carlo method. The proposed FRPD method was applied to evaluate the fatigue failure probability of central I-type crack square plates, through which the accuracy and efficiency of the proposed method were verified against analytical results. The influence of the shielding effect on the SIF was also well captured in the simulation.
(3) The fatigue performance of the Ting Kau Bridge was evaluated using the proposed method. It was found that all the steel stringers

with central cracks can meet the requirement of a design life of 120 years with a target reliability index $\beta = 3.5$. While in the case of a single-sided crack, only half of the steel stringers and one steel girder can satisfy the requirement. The example illustrates that the proposed method has good potential for the fatigue analysis of steel bridges.

Future research will focus on the further verification of this method through applications to other types of bridges.

## Declaration of Competing Interest

The authors declare that they have no known competing financial interests or personal relationships that could have appeared to influence the work reported in this paper.

## Acknowledgment

Support for this work from Hunan Provincial Innovation Foundation for Postgraduate (CX2018B221) is gratefully acknowledged.

## Appendix A. Supplementary material

Supplementary data to this article can be found online at https://doi.org/10.1016/j.engfracmech.2020.107214.

## References

[1] Imam BM, Righiniotis TD. Fatigue evaluation of riveted railway bridges through global and local analysis. Constr Steel Res 2010;66(11):1411–21.
[2] Helmerich R, Kühn B, Nussbaumer A. Assessment of existing steel structures. A guideline for estimation of the remaining fatigue life. Struct Infrastruct Engng 2007;3(3):245–55.
[3] Adasooriya ND, Siriwardane SC. Remaining fatigue life estimation of corroded bridge members. Fatigue Fract Engng Mater Struct 2014;37(6):603–22.
[4] Li ZX, Chan THT, Ko JM. Determination of effective stress range and its application on fatigue stress assessment of existing bridges. Int J Solids Struct 2002;39(9):2401–17.
[5] Li ZX, Chan THT. Fatigue criteria for integrity assessment of long-span steel bridge with health monitoring. Theor Appl Fract Mech 2006;46(2):114–27.
[6] Maljaars J, Steenbergen HMGM, Vrouwenvelder ACWM. Probabilistic model for fatigue crack growth and fracture of welded joints in civil engineering structures. Int J Fatigue 2012;38:108–17.
[7] Battista RC, Pfeil MS, Carvalho EML. Fatigue life estimates for a slender orthotropic steel deck. J Constr Steel Res 2008;64(1):134–43.
[8] Fonseca DOC, Jose A, Silva P, et al. Fatigue Strength Evaluation of Resin-Injected Bolted Connections Using Statistical Analysis. Engineering 2017;3(6):795–805.
[9] Wang W, Deng L. Impact Factors for Fatigue Design of Steel I-Girder Bridges Considering the Deterioration of Road Surface Condition. J Bridg Eng 2016;21(5):04016011.
[10] Zhang W, Asce SM, Cai CS, Asce F. Fatigue Reliability Assessment for Existing Bridges Considering Vehicle Speed and Road Surface Conditions. J Bridg Eng 2012;17(3):443–53.
[11] Deng L, Cai CS. Development of dynamic impact factor for performance evaluation of existing multi-girder concrete bridges. Engng Struct 2010;32(1):21–31.
[12] Tabatabai H, Hawileh R, Rahman A. A non-linear 3D FEM to simulate un-bonded steel reinforcement bars under axial and bending loads. Engineering 2009;1(2):75–90.
[13] Deng L, Wang W, He XH. Optimization and application of fatigue design based on AASHTO code. China J Highw Transp 2017;30(3):40–8.
[14] Deng L, Bi T, He W, Wang W. Vehicle weight limit analysis method for reinforced concrete bridges based on fatigue life. China J Highw Transp 2017;30(4):72–8.
[15] Bolzon G, Corigliano A. Finite elements with embedded displacement discontinuity: a generalized variable formulation. Int J Numer Meth Engng 2000;49(10):1227–66.
[16] Stazi FL, Budyn E, Chessa J, Belytschko T. An extended finite element method with higher-order elements for curved cracks. Comput Mech 2003;31(1–2):38–48.
[17] Shen F, Zhang Q, Huang D. Damage and failure process of concrete structure under uniaxial compression based on Peridynamics modeling. Math Probl Eng 2013:631074.
[18] Feng Y, Mei D, Wang Y. Cohesive zone method based multi particle finite element simulation of compaction densification process of Al and NaCl laminar composite powders. J Phys Chem Solids 2019;134:35–42.
[19] Silling SA. Reformulation of elasticity theory for discontinuities and long-range forces. J Mech Phys Solids 2000;48:175–209.
[20] Ballarini R, Diana V, Biolzi L, Casolo S. Bond-based peridynamic modelling of singular and nonsingular crack-tip fields. Meccanica 2018;53(14):3495–515.
[21] Cheng Z, Liu YK, Zhao J, Feng H, Wu Y. Numerical simulation of crack propagation and branching in functionally graded materials using peridynamic modeling. Engng Fract Mech 2018;191:13–32.
[22] Chen Z, Bobaru F. Peridynamic modeling of pitting corrosion damage. J Mech Phys Solids 2015;78:352–81.
[23] Silling SA, Askari A. Peridynamic model for fatigue cracks. Sandia Rep 2014;SAND2014-1.
[24] Oterkus E, Guven I, Madenci E. Fatigue failure model with peridynamic theory. In: 2010 12th IEEE Intersoc Conf Therm Thermomechanical Phenom Electron Syst ITherm. 2010.
[25] Jung J, Seok J. Mixed-mode fatigue crack growth analysis using peridynamic approach. Int J Fatigue 2017;103:591–603.
[26] Ha YH, Bobaru F. Characteristics of dynamic brittle fracture captured with peridynamics. Engng Fract Mech 2011;78(6):1156–68.
[27] Manshadi FD, Mikaili S, Gorji IF. Ultrasonic thickness of middle trapezius muscle in young healthy men. J Maz Univ Med Sci 2017;27:148–53.
[28] Zhang G, Le Q, Loghin A, SubramaniyanA BF. Validation of a peridynamic model for fatigue cracking. Engng Fract Mech 2016;162:76–94.
[29] Hu W, Ha YD, Bobaru F, Silling SA. The formulation and computation of the nonlocal J-integral in bond-based peridynamics. Int J Fract 2012;176(2):195–206.
[30] Du Q, Tao Y, Tian X. A Peridynamic Model of Fracture Mechanics with Bond-Breaking. J Elast 2018;132(2):197–218.
[31] Zhao T, Jiang Y. Fatigue of 7075–T651 aluminum alloy. Int J Fatigue 2008;30(5):834–49.
[32] Rackwitz R, Fiessler B. Structural reliability under combined random load sequences. Comput Sruct 1978;9(5):489–94.
[33] Breitbarth E, Besel M. Fatigue crack deflection in cruciform specimens subjected to biaxial loading conditions. Int J Fatigue 2018;113:345–50.
[34] Paris PC, Sih GC. Fracture toughness testing and its applications. Am Soc Testing Mater 1965:63–77.
[35] Leguillon D, Murer S. Crack deflection in a biaxial stress state. Int J Fracture 2008;150(1–2):75–90.
[36] Duan M, Li Y, Liu H, Shu Y. Fatigue crack behaviors under asynchronous biaxial loading. Int J Fatigue 2019;136:248–57.
[37] Shojaei A, Mossaiby F, Zaccariotto M, Galvanetto U. An adaptive multi-grid peridynamic method for dynamic fracture analysis. Int J Mech Sci 2018;144:600–17.
[38] Wallin K. The scatter in KIC-results. Engng Fract Mech 1984;19(6):1085–93.
[39] Bullough R, Green VR, Tomkins B, et al. A review of methods and applications of reliability analysis for structural integrity assessment of UK nuclear plant. Int J Press Vessel Pip 1999;76(13):909–19.

[40] Riahi H, Bressolette P, Chateauneuf A. Random fatigue crack growth in mixed mode by stochastic collocation method. Engng Fract Mech 2010;77(16):3292–309.
[41] Liu WK, Chen Y, Belytschko T, et al. Three reliability methods for fatigue crack growth. Engng Fract Mech 1996;53(5):733–52.
[42] J. Newman JC. An improved method of collocation for the stress analysis of cracked. Hampton, Virginia, 1971.
[43] Panchadhara R, Gordon PA. Application of peridynamic stress intensity factors to dynamic fracture initiation and propagation. Int J Fract 2016;201(1):81–96.
[44] Luo P. Establishment of bridge rating systems for Ting Kau Bridge - Statistical modelling and simulation of predominant highways loading effects. Hong Kong: Highways Department Bridges and Highways Division; 2009.
[45] Qing F, Au FTK. Establishment of bridge rating systems for Ting Kau Bridge - criticality and vulnerability analysis fatigue damage and fatigue life. Hong Kong: Highways Department Bridges and Highways Division; 2010.
[46] Li SH, Ren JY. Analytical study on dynamic responses of a curved beam subjected to three-directional moving loads. Appl Math Model 2018;58:365–87.
[47] Arya C. Eurocode 3: Design of steel structures. Design Struct Elements 2009.
[48] Xu G, Yang R, Zhou K, Fan X. Methodology to estimate remaining service life of steel structure by possibilistic reliability theory. Chinese J Mech Eng (Eng Ed) 2010;23(6):780–7.
[49] BS 5400 Part 10 1980, Steel, concrete and composite bridges – Part 10. UK: British Standards Institution 1980.